RSC Advances

PAPER

View Article Online
View Journal | View Issue

Cite this: *RSC Adv.*, 2023, **13**, 10940

Synthesis of magnetic graphene-like carbon nitride-cobalt ferrite (g-C_3N_4/$CoFe_2O_4$) nanocomposite for sonocatalytic remediation of toxic organic dyes

Saeedeh Hassanzadeh, Saeed Farhadi * and Farzaneh Moradifard

A novel magnetic g-C_3N_4/$CoFe_2O_4$ nanocomposite was successfully synthesized by a simple hydrothermal method and applied as a new graphene-like carbon nitride-based sonocatalyst for sonodegradation of pollutant dyes. The as-prepared samples were characterized by using X-ray diffraction (XRD), Fourier transform infrared (FT-IR) spectroscopy, field-emission scanning electron microscopy (FE-SEM), energy-dispersive X-ray spectroscopy (EDX), transmission electron microscopy (TEM), vibrating sample magnetometry (VSM), X-ray photoelectron spectroscopy (XPS), UV-visible diffuse reflectance spectroscopy (DRS), BET surface area measurements and photoluminescence (PL) spectroscopy. The results indicate that the nanocomposite sample is composed of spherical $CoFe_2O_4$ nanoparticles adhered to g-C_3N_4 naosheets. The g-C_3N_4/$CoFe_2O_4$ nanocomposites were used as a new magnetically separable sonocatalyst in H_2O_2-assisted sonodegradation of methylene blue (MB), rhodamine B (RhB) and methyl orange (MO) dyes in aqueous media. The results showed complete degradation (*ca.* 100%) of dyes within short times (30–35 min). The sonocatalytic activity of graphitic carbon nitride (g-C_3N_4) was greatly enhanced with $CoFe_2O_4$ modification. Trapping experiments indicated that the g-C_3N_4/$CoFe_2O_4$ nanocomposites serves as a generator of hydroxyl radical ($^{\bullet}OH$) *via* activation of H_2O_2 for degradation of dyes under ultrasound irradiation. Furthermore, the magnetic sonocatalyst can be separated from solution by an external magnet and reused several times without observable loss of activity. The possible mechanism of sonocatalytic activity was also proposed according to experimental results.

Received 4th January 2023
Accepted 3rd April 2023

DOI: 10.1039/d3ra00057e

rsc.li/rsc-advances

1. Introduction

Environmental pollution resulting from industrial wastewater containing various organic dyes is getting more and more serious with the rapid development of economy and society.[1,2] Among various techniques, advanced oxidation processes (AOPs) such as ozonation, photolysis, Fenton process and photocatalytic oxidation have recently received a particular interest as they display a high efficacy in wastewater treatment.[3–6] Among AOPs, the photo-catalytic degradation of organic pollutants in the presence of semiconductors has attracted considerable interest because it is a promising environmental and cost-effective AOP for the treatment of contaminated groundwater and wastewater.[3–6] However, organic dye wastewaters are highly concentrated and typically non-transparent. Consequently, light penetration is limited to only several millimetres, thereby affecting the efficacy of semiconductor photocatalyst to achieve complete degradation of such wastewaters. To meet the fast-developing water treatment requirements, there is a great need to devise innovative technologies and materials for efficient removal of pollutants from non-transparent wastewater. As a potential alternative to conventional AOPs, sonolysis by using ultrasound irradiation is of great interest and importance because of environment-friendly and simply operating.[7,8]

In recent years, ultrasound (US)-assisted degradation has attracted considerable attention for the elimination of various organic pollutants owing to its several advantages such as operational simplicity, safety and being environmentally benign.[9–11] This technique is principally based on the phenomenon of acoustic cavitation including nucleation, growth, and violent collapse of micro-bubbles, leading to the emission of sonoluminescence (SL) and generation of 'hot spot' with extremely high temperature and pressure (~5000 °C and ~1000 atm). As a result, water is dissociated to generate hydroxyl radicals, which can oxidize organic pollutants into CO_2 and H_2O.[12–15] Moreover, organic pollutant that is volatile or hydrophobic appears to diffuse inside the cavity interior and undergoes the pyrolytic reaction directly.[16–20] However, to obtain a fast-degradation rate using ultrasound (US) alone typically requires a significant amount of electrical energy owing to the

Department of Chemistry, Lorestan University, Khorramabad 68151-44316, Iran. E-mail: farhadi.s@lu.ac.ir; Fax: +986633120618; Tel: +986633120611

massive loss of input energy in thermal dissipation, which hinders the wide application of sonolysis for practical water treatment.[21] To overcome this problem, development of semiconductor-based sonocatalysis is one of the most promising strategies. Similar with photocatalysis, the sonocatalytic degradation of some organic dyes in aqueous solution is also an excellent method. Nano-TiO_2 powder is known to exhibit very high sonocatalytic activities in treating various organic dyes in wastewaters. In addition, heterogeneous sonocatalysis can overcome the aforementioned disadvantages of the photocatalytic technology because ultrasonic irradiation has strong penetration ability in all types of water media.[22] Up till now, a variety of sonocatalysts have been reported to exhibit very high sonocatalytic activities in treating various organic dyes in wastewaters.[23–25] It is well known that the sonocatalytic efficiency depends highly on the type of catalyst.[26] Therefore, the development of novel efficient and green sonocatalysts is important to promote sonocatalysis-based applications and further understand the sonocatalysis mechanism.

Graphitic carbon nitride (g-C_3N_4) with a graphene-like structure as a metal-free and visible-light-responsive photocatalyst and its composites have drawn considerable attention because of its appealing electronic band structure, highly physicochemical stability, and earth-abundant merits.[27] However, its photocatalytic performance is currently narrowed by the nonresponse in the long wavelength region, poor electrical transport, low density of reactive sites, and high recombination of photoexcited electron–hole pairs.[28,29] Besides, pure g-C_3N_4 photocatalyst and its non-magnetic composites are difficult to be separated and recycled from wastewater and easily produces secondary pollution, which limits the practical application of g-C_3N_4.[30–32] The Fe-based spinel metal ferrite systems with the general molecular structure MFe_2O_4 (M = Ni, Zn, Co, Ca, Mn, Mg, and Cu) have gained technological importance in photocatalysis due to their highly visible light utilization, low band gap, high-temperature stability, and extraordinary chemical stability.[33] In recent years, the coupling between spinel metal ferrites MFe_2O_4 (M = Ni, Zn, Co, and Cu) and g-C_3N_4 has been widely studied in photocatalytic energy and environmental remediation fields due to their suitable band structure for effective separation of charge carriers.[34–41] Moreover, the magnetic nature of the spinel ferrites helps to recover the catalyst after the photocatalytic reaction. However, up to now, the investigation of g-C_3N_4/MFe_2O_4 as advanced sonocatalyst has rarely been reported.[24]

In the present study, a novel magnetically separable graphite-like carbon nitride (g-C_3N_4)-based sonocatalyst (g-C_3N_4/$CoFe_2O_4$) was prepared by a facile hydrothermal route. The composition, microstructure, magnetic and optical properties of the synthesized nanocomposite were fully characterized by various physical techniques. Its sonocatalytic activity was assessed by the H_2O_2-assisted degradation of organic dyes in water under ultrasound irradiation. The effects of various parameters (*e.g.* H_2O_2 quantity, the catalyst dosage, and initial dye concentration) on the sonodegradation process were investigated. The sonocatalytic activity of g-C_3N_4/$CoFe_2O_4$ nanocomposite was also compared with those of pure $CoFe_2O_4$ and g-C_3N_4 under similar conditions. In addition, a possible mechanism for activity of the nanocomposite under ultrasound irradiation was proposed.

2. Experimental

2.1. Materials

Thiourea (CH_4N_2S, 98%), iron(III) nitrate nonahydrate ($Fe(NO_3)_3 \cdot 9H_2O$, 99%), cobalt nitrate hexahydrate ($Co(NO_3)_2 \cdot 6H_2O$, 99%), hydrogen peroxide (H_2O_2, 30%), methylene blue (MB, $C_{16}H_{18}ClN_3S$, 98%) and methyl orange (MO, $C_{14}H_{14}N_3NaO_3S$, 98%) and rhodamine B (RhB, $C_{28}H_{31}N_2O_3Cl$, 98%) were prepared from Merck chemical company and used as received without more purification. Deionized and doubly distilled water were used throughout this study.

2.2. Characterization techniques

The phase formation in the composites was investigated *via* powder X-ray diffraction (XRD) technology on a Panalytical X'Pert Pro diffractometer (Netherlands) with Cu Kα ($\lambda = 1.5406$ Å) at 40 kV and 150 mA. Diffraction patterns in the 10–80° regions were recorded at a rate of 5°/min. The chemical composition and chemical bonding state of the specimen were defined by X-ray photoelectron spectroscopy (XPS, equipped with a standard monochromatic Al Kα source ($h\nu$) 1486.6 eV, ESCALAB 250Xi, Thermo Fisher Scientific, UK). Fourier Transform Infrared (FT-IR) spectra were recorded on a Shimadzu 160 spectrophotometer (Japan) from 500 to 4000 cm^{-1} using KBr pellets. The morphology and elemental analysis of the g-C_3N_4/$CoFe_2O_4$ nanocomposite were observed by on a field emission scanning electron microscopy (FESEM, Mira3 Tescan, Czech) equipped with a link energy-dispersive X-ray analyzer. Transmission electron microscopy (TEM) images were taken on EM10C electron microscope operating at 100 kV. The Brunauer–Emmett–Teller (BET) analysis was performed by a PHS-1020 PHSCHINA instrument to obtain the specific surface area and porosity of g-C_3N_4/$CoFe_2O_4$ nanocomposite. The UV-vis spectra of dye solutions were analyzed at room temperature using a Cary 100 UV visible spectrophotometer. The room-temperature magnetic properties were measured by a 7400-S vibrating sample magnetometer (VSM, Daneshpajoh Kashan Co, Iran) with a maximum magnetic field of 10 kOe. The UV-vis diffuse reflectance spectra (DRS) of sonocatalysts were obtained on a Sinico S4100 spectrophotometer using $BaSO_4$ powder as a standard. The loading amount of $CoFe_2O_4$ in the composite adsorbent and the concentrations of Co and Fe metals in the filtrates and solutions after recovering photocatalyst were determined by inductively coupled plasma atomic emission spectrometer (PerkinElmer ICP-AES, USA).

2.3. Preparation of the g-C_3N_4 nanosheets

In a typical synthesis, 10 g of thiourea powder was put into a porcelain crucible with a cover, and then heated to 550 °C at a heating rate of 15 °C min in a furnace for 2 h in air. The resulted yellow powder (g-C_3N_4) was collected and washed with

0.1 M HNO_3 and distilled water, and it was dried to 60 °C in the oven for 12 h.

2.4. Preparation of the magnetic g-C_3N_4/$CoFe_2O_4$ nanocomposite

The g-C_3N_4/$CoFe_2O_4$ nanocomposite was synthesized *via* a hydrothermal route. 23 mg of the obtained g-C_3N_4 was dispersed into a 25 mL aqueous solution containing stoichiometric amounts of cobalt(II) and iron(III) nitrates (containing 17 mg of $CoFe_2O_4$) under sonication for 30 min. The pH value of the mixture was adjusted to 11 with a 6 mol L^{-1} NaOH aqueous solution. After 1 h of stirring, the resulting mixture was transferred and sealed into a 50 mL Teflon-lined stainless-steel autoclave and heated at 180 °C for 12 h. After naturally cooling down to room temperature, the resulting product was filtered and rinsed with distilled water and ethanol, followed by drying at 60 °C overnight. The loading amount of $CoFe_2O_4$ in the nanocomposite was estimated to be about 38 wt% by ICP-AES analysis. For comparison purposes, the pure $CoFe_2O_4$ nanoparticles were also synthesized under the same experimental conditions without adding the g-C_3N_4. The preparation process of the g-C_3N_4/$CoFe_2O_4$ nanocomposite was summarized in Scheme 1.

2.5. Sonocatalytic degradation of organic dyes

The sonocatalytic performance of the as-prepared g-C_3N_4/$CoFe_2O_4$ nanocomposite was evaluated *via* the degradation of organic dyes in aqueous solutions at 25 ± 2 °C using an ultrasonic bath (Sonic 6MX, England) under an output power of 100 W and frequency of 37 kHz. In a typical experiment, 50 mL of an aqueous solution containing MB dye (30 mg L^{-1}), 25 mg of the g-C_3N_4/$CoFe_2O_4$ nanocomposite powder and 0–2.5 mL of H_2O_2 (0.1 mol L^{-1}) were added into a 100 mL Pyrex cylindrical vessel. The mixture was vigorously stirred for 30 min to establish the adsorption–desorption equilibrium. Then, it was exposed to ultrasonic irradiation. The sonocatalytic system was

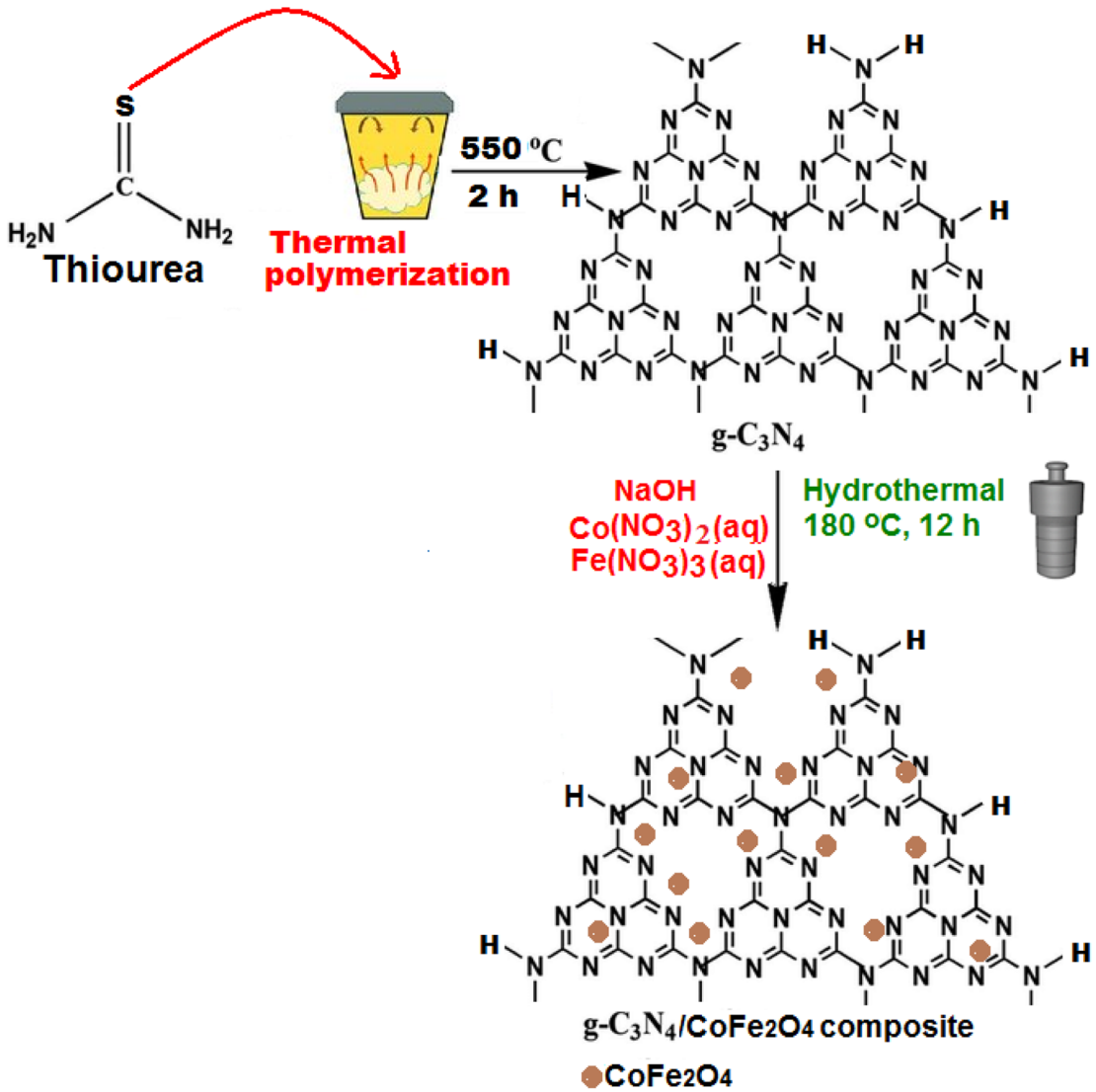

Scheme 1 The preparation process of the g-C_3N_4/$CoFe_2O_4$ nanocomposite.

maintained at room temperature by a flow of cooling water during the reaction. At regular time intervals, 2 mL of samples of the reaction solution were separated, and the catalyst powder was immediately separated from the suspension with an external magnet, washed and dried at 80 °C for the next runs. Then, the residual MB concentration in solutions was determined using a UV-vis spectrophotometer at wavelength of 664 nm. The degradation efficiency (DE) was calculated as follow: DE (%) = $[(C_0 - C_t)/C_0] \times 100\%$, where C_0 is the initial concentration of dye and C_t is the time-dependent concentration of dye upon irradiation. The effects of parameters including the H_2O_2 amount (0.1 mol L; 0, 0.5, 1, 1.5, 2 and 2.5 mL), sonocatalyst dosage (0, 0.33, 0.66, 0.83, 1 g L^{-1}), initial dye concentration (25, 30, 35, 50 mg L^{-1}) and initial solution pH (3, 7, 9) were also studied on the sonocatalytic efficiency of the g-C_3N_4/$CoFe_2O_4$ nanocomposite with 0.1 mol L^{-1} HCl and NaOH aqueous solutions. The sonodegradation of methyl orange (MO) and Rhodamine B (RhB) dyes were also conducted under the same conditions.

3. Results and discussion

3.1. Characterization of the g-C_3N_4/$CoFe_2O_4$ sonocatalyst

Fig. 1 shows the IR spectra of $CoFe_2O_4$, g-C_3N_4 and g-C_3N_4/$CoFe_2O_4$ composite. The FT-IR spectrum in Fig. 1(a) shows all the characteristic bands of pure g-C_3N_4 phase. The characteristic band at about 810 cm^{-1} is attributed to the characteristic breathing mode of s-triazine units.[42,43] The other several bands ranging from 1100 to 1650 cm^{-1} can be attributed to the typical stretching mode of C–N heterocycles in g-C_3N_4.[44,45] The broad bands at around 3000–3500 cm^{-1} correspond to the secondary and primary amines at the defect sites of the aromatic ring.[46] In Fig. 1(b), the characteristic band at around 580 cm^{-1}

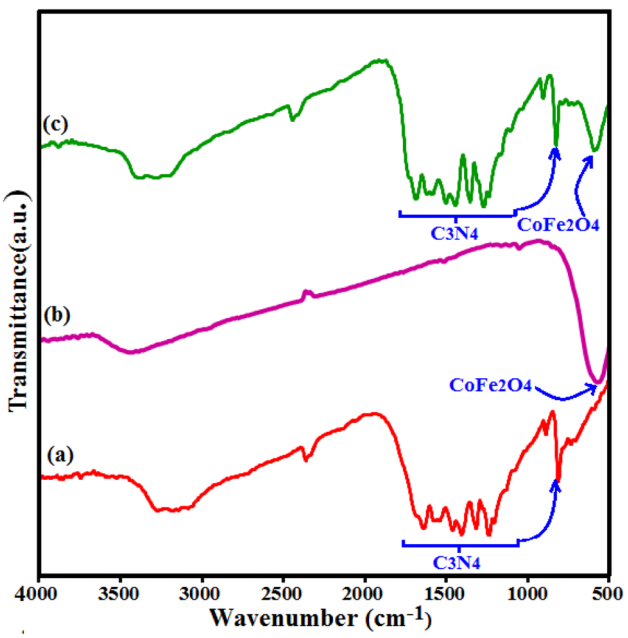

Fig. 1 FT-IR spectra of (a) C_3N_4, (b) $CoFe_2O_4$ and (c) g-C_3N_4/$CoFe_2O_4$ samples.

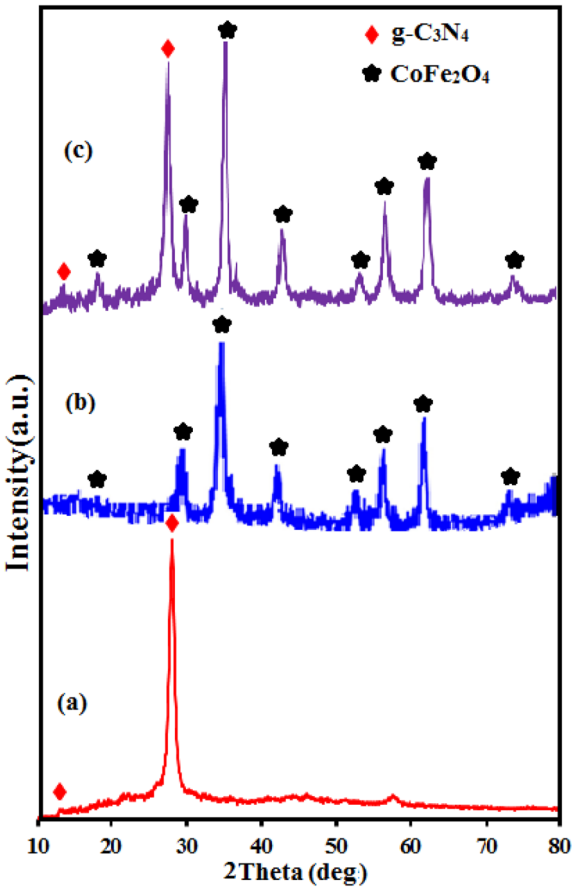

Fig. 2 XRD patterns of (a) g-C_3N_4, (b) $CoFe_2O_4$ and (c) g-C_3N_4/$CoFe_2O_4$ samples.

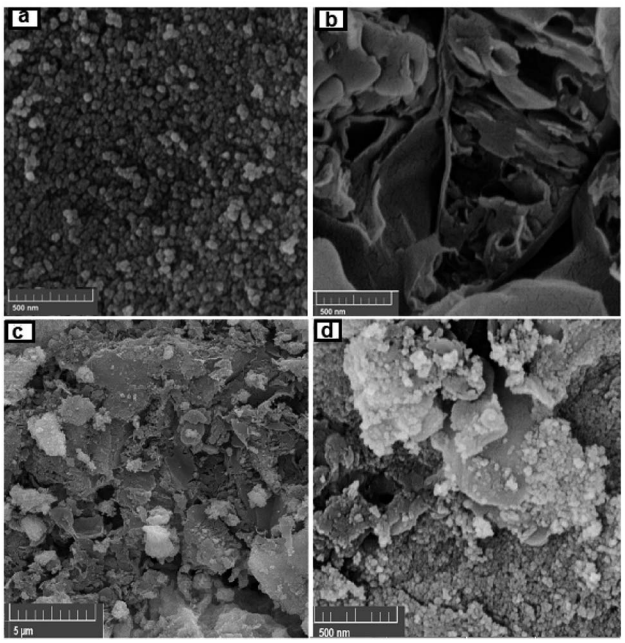

Fig. 3 FE-SEM images of (a) $CoFe_2O_4$, (b) g-C_3N_4, and (c and d) the g-C_3N_4/$CoFe_2O_4$ hybrid nanocomposite.

corresponds to the stretching vibration of Fe–O bond of spinel-type $CoFe_2O_4$ nanoparticles.[47] FT-IR spectrum of the g-C_3N_4/$CoFe_2O_4$ nanocomposite in Fig. 1(c) shows characteristic bands correspond to the C_3N_4 at 1100–1650 and 810 cm^{-1}, besides the strong band of $CoFe_2O_4$ at about 580 cm^{-1}. This finding demonstrates the coexistence of g-C_3N_4 and $CoFe_2O_4$ after the formation of g-C_3N_4/$CoFe_2O_4$ nanocomposite Fig. 2 shows the XRD patterns of the pristine C_3N_4, pure $CoFe_2O_4$ and g-C_3N_4/$CoFe_2O_4$ samples.

The XRD pattern of C_3N_4 in Fig. 2(a) shows two characteristic peaks of g-C_3N_4 at 13.1° and 27.3°. The weak peak at $2\theta = 13.1°$ is corresponds to the (100) diffraction peak, which relates to the interplanar structural packing with a period of 0.675 nm and the strong peak at $2\theta = 27.3°$ can be indexed as the (002) diffraction peak and represents the interplanar graphitic stacking with a distance of the two near layers of 0.325 nm.[48] All diffraction peaks appeared in Fig. 2(b) at 2θ angles of 30.3°, 35.5°, 37.1°, 43.2°, 53.6°, 57.3°, 62.8° and 72° can be indexed as the (111), (220), (311), (222), (400), (511), (440) and (441) planes

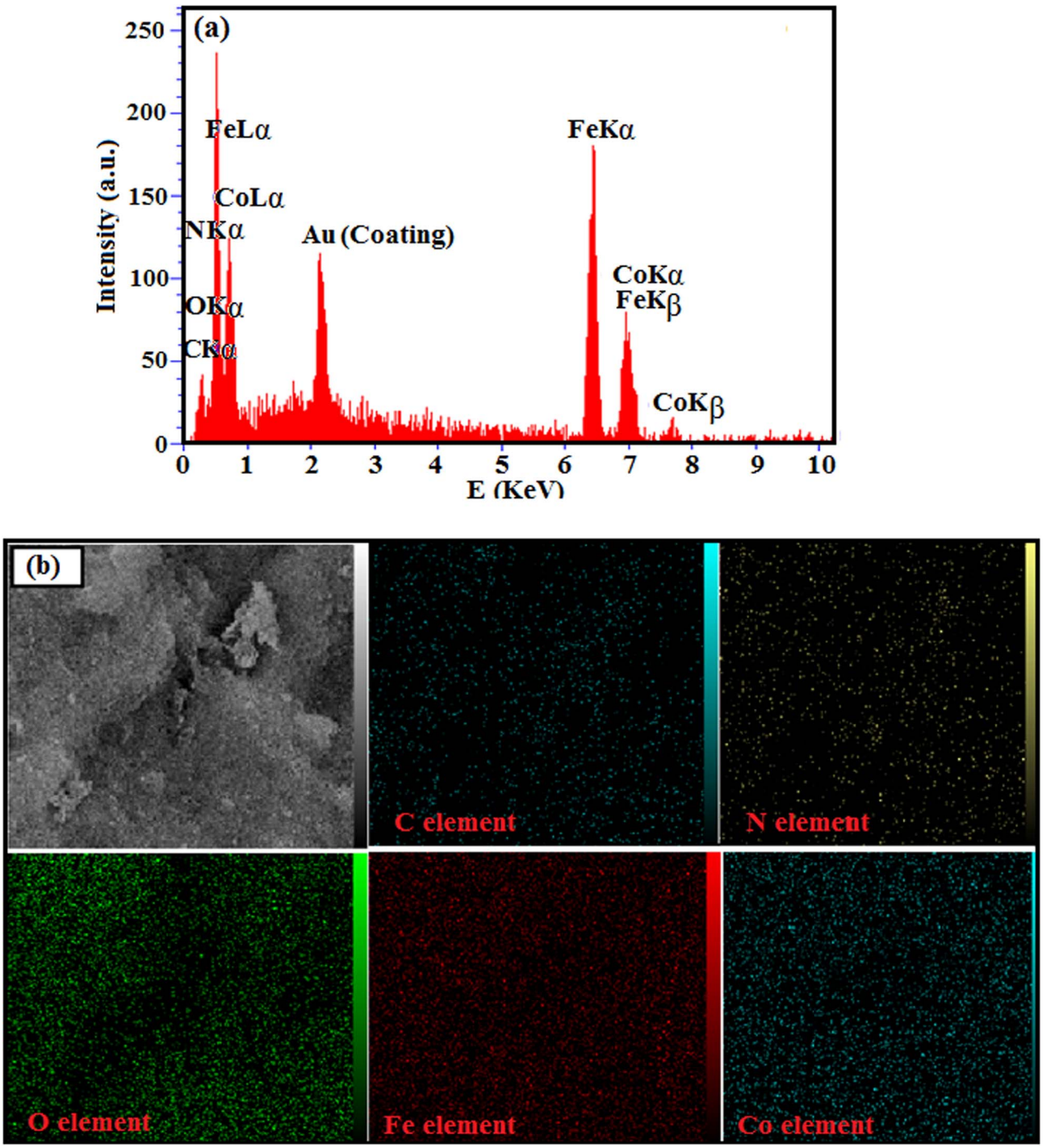

Fig. 4 (a) The EDX spectrum and (b) elemental mappings of g-C_3N_4/$CoFe_2O_4$ nanocomposite.

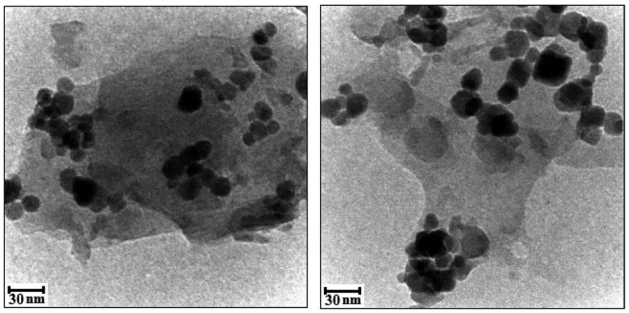

Fig. 5 The TEM images of the g-C_3N_4/$CoFe_2O_4$ nanocomposite.

of the cubic structure of $CoFe_2O_4$ (JCPDS no. 10-0454), respectively.[37] The XRD pattern of the g-C_3N_4/$CoFe_2O_4$ composite in Fig. 2(c) exhibits the characteristic diffraction peaks of both g-C_3N_4 and $CoFe_2O_4$ phases, indicating the coexistence of g-C_3N_4 and $CoFe_2O_4$ phases without any impurity phase.[49] The average particle size of $CoFe_2O_4$ in the nanocomposite by using the Debye–Scherrer equation was estimated to be 20 nm.

SEM images indicating the morphology of g-C_3N_4, $CoFe_2O_4$ and g-C_3N_4/$CoFe_2O_4$ nanocomposite samples are shown in Fig. 3. SEM image of pure g-C_3N_4 in Fig. 3(a) shows layered structure of g-C_3N_4 having large stacks, possibly consisting of hundreds of graphene-like nanosheets. It should also be noted that the surfaces of g-C_3N_4 sheets were quite flat and smooth. The SEM image of $CoFe_2O_4$ sample in Fig. 3(b) shows nearly

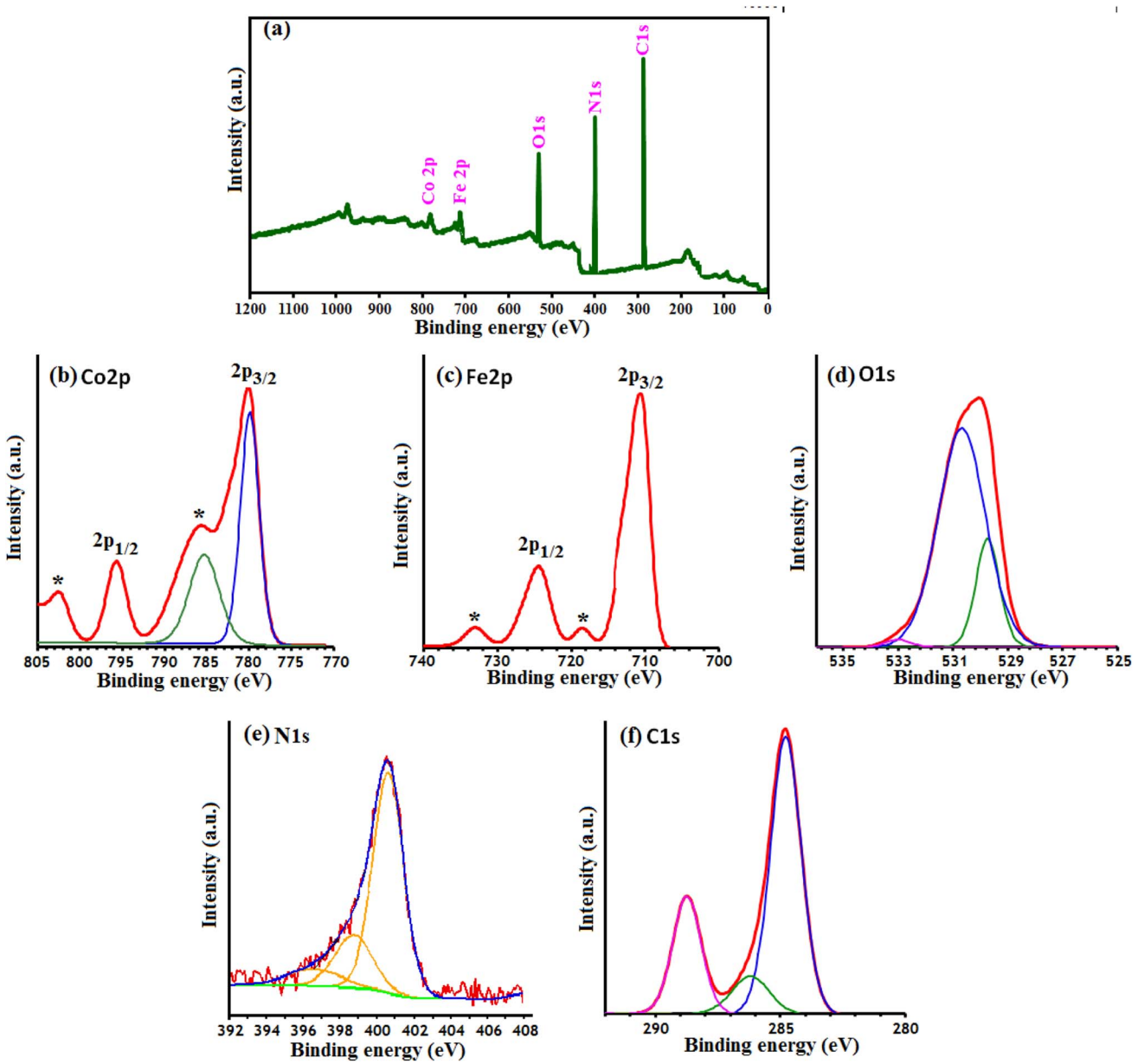

Fig. 6 XPS of the g-C_3N_4/$CoFe_2O_4$ nanocomposite: (a) survey spectrum, (b) Co 2p spectrum, (c) Fe 2p spectrum, (d) O 1S spectrum, (e) N 1S spectrum and (f) C 1S spectrum.

uniform monodispersed sphere-like nanoparticles with an average diameter of about 20 nm. The SEM images of g-C_3N_4/$CoFe_2O_4$ in Fig. 3(c) and (d) clearly show C_3N_4 nanosheets were successfully decorated with $CoFe_2O_4$ nanoparticles. It can be clearly seen that the $CoFe_2O_4$ nanoparticles were well deposited on g-C_3N_4. Some wrinkles are found on the surface, which may be important for preventing aggregation of g-C_3N_4 and maintaining high surface area, which could be a great benefit to its adsorption ability. On the contrary with pure g-C_3N_4 sheets, the surface of g-C_3N_4 nanosheets in the nanocomposite was rough and the edges were highly crumpled.

The chemical composition and homogeneity of g-C_3N_4/$CoFe_2O_4$ nanocomposite was further confirmed by EDX analysis and the results are shown in Fig. 4. The EDX spectrum of the nanocomposite in Fig. 4(a) shows the peaks of C, N, Co, Fe, and O elements at their corresponding keV values. The distribution of elements present in the nanocomposite was studied using SEM-EDX mapping analysis as shown in Fig. 4(b). The elemental mappings show all elements were uniformly distributed over the nanocomposite, confirming the homogeneity of the sample.

The morphologies and microstructures of the as-prepared g-C_3N_4/$CoFe_2O_4$ samples were further analyzed by TEM. As can be seen in Fig. 5, the almost transparent graphene-like g-C_3N_4 sheets are fully exfoliated and decorated with black color $CoFe_2O_4$ sphere-like nanoparticles with having the particle size in range of 15–30 nm in consistent with the average particle size calculated from Debye-Scherer formula. No obvious aggregation was seen in images. The g-C_3N_4 sheets could not only prevent agglomeration of the $CoFe_2O_4$ nanoparticles and enable a good dispersion of these spherical particles, but also substantially enhance the specific surface area of the composite.

XPS analysis was carried out to determine the surface composition and oxidation states of the as-prepared g-C_3N_4/$CoFe_2O_4$ nanocomposite. As shown in Fig. 6(a), C, N, Co, Fe and O elements can be readily indexed in the XPS survey spectrum of the nanocomposite. Among them, the intensity of the Co and Fe elements is relatively low, which indicates that only a small amount of $CoFe_2O_4$ nanoparticles are distributed on the surface of the composite sample. The high resolution XPS spectrum of Co 2p (Fig. 6(b)) reveals four peaks located at 782.3 eV, 787.7 eV (a satellite peak), 796.49 eV and 804.72 eV (a satellite peak), respectively, implying that Co element exists mainly in the chemical state of Co^{2+}.[50,51] The Fe 2p spectrum of $CoFe_2O_4$ is composed of two distinct peaks at 711.8 eV and 725.2 eV (Fig. 6(c)) and the two peaks ascribed to the Fe $2p_{3/2}$ and Fe $2p_{1/2}$, respectively, which is in good agreement with the reported value for Fe^{3+} compounds.[52–54] Furthermore, two satellite peak of the Fe 2p can also be detected at the position of 719.1 and 733 eV. In Fig. 6(d), the XPS peaks of the O 1s were observed at 530.40 eV and 531.83 eV, which was ascribed to crystal lattice oxygen (Co–O and Fe–O) and surface OH/H_2O groups, respectively.[55] N 1s XPS spectrum in Fig. 6(e) can be deconvoluted into three main peaks at 399.4, 401.2, and 403.4 eV, which correspond to C–N–C, N–(C)3, and NH/NH_2 groups of g-C_3N_4, respectively.[56] In Fig. 6(f), the first C 1s peak at 288.5 eV was assigned to sp^2-bonded carbon (N–C=N), and the second at 284.8 eV was attributed to graphitic carbon which was usually observed on carbon nitrides.[56]

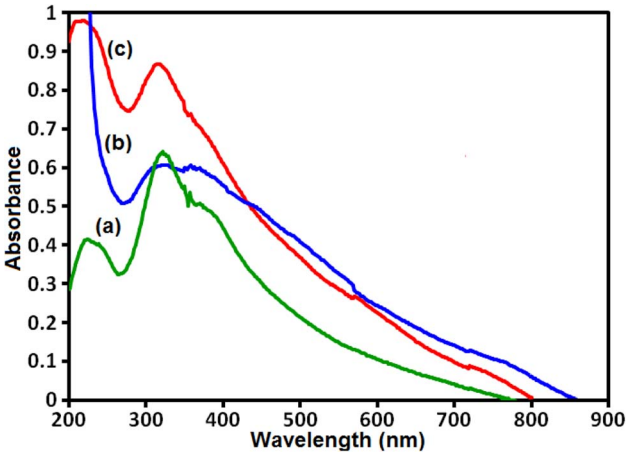

Fig. 7 UV-vis DRS spectra of (a) g-C_3N_4, (b) $CoFe_2O_4$ and (c) g-C_3N_4/$CoFe_2O_4$ nanocomposite.

The UV-vis diffuse reflectance spectra (UV-vis DRS) was used to investigate the optical absorption properties of samples and results are shown in Fig. 7. The UV-vis spectrum of pure g-C_3N_4 sample in Fig. 7(a) shows a strong absorption band from the UV to the visible light region with a maximum absorption at about 450 nm. The UV-vis spectrum of $CoFe_2O_4$ sample in Fig. 7(b) exhibits a broad absorption band in the visible range. As can be seen in Fig. 7(c), the UV-vis spectrum of g-C_3N_4/$CoFe_2O_4$ nanocomposite indicates an enhancement in absorption intensity in the visible region together with a red shift, compared to that of the pure g-C_3N_4, and this was attributed to $CoFe_2O_4$ nanoparticles assembled on the surface of g-C_3N_4 nanosheets that acts as a sensitizer to extend the optical response. The absorption bands are used for the calculation of band gaps (E_g) of these samples according to the Tauc's equation:[57] $(\alpha h\nu)^2 = B(h\nu - E_g)$, where α, ν, and B are absorption coefficient, light frequency and proportionality constant, respectively. The Eg of g-C_3N_4, $CoFe_2O_4$ and g-C_3N_4/$CoFe_2O_4$ nanocomposite were estimated with extrapolation of the plots of $(\alpha h\nu)^2$ against $h\nu$ to the energy axis. The E_g values of g-C_3N_4, $CoFe_2O_4$ and g-C_3N_4/$CoFe_2O_4$ samples were calculated to be 2.7, 1.3 and 2.5 eV, respectively. These results suggest that the g-C_3N_4/$CoFe_2O_4$ composite can absorb visible-light photons more efficient than pure g-C_3N_4. Obviously, the visible light absorption intensity of g-C_3N_4/$CoFe_2O_4$ heterojunction is better than that of g-C_3N_4, which possibly results good visible-light utilization.

The magnetization curves of the $CoFe_2O_4$ and g-C_3N_4/$CoFe_2O_4$ samples under an applied magnetic field of ±10 kOe at room temperature are shown in Fig. 8. The magnetic hysteresis loops of the samples indicate ferromagnetic behaviors, due to the presence of $CoFe_2O_4$ nanoparticles. The saturation magnetization (Ms) of pure $CoFe_2O_4$ is 62.8 emu g^{-1} (Fig. 8(a)). The Ms of g-C_3N_4/$CoFe_2O_4$ nanocomposite is about 28.4 emu g^{-1} (Fig. 8(b)). The Ms of the magnetic nanocomposite decreased considerably, compared with that of pure $CoFe_2O_4$, which can

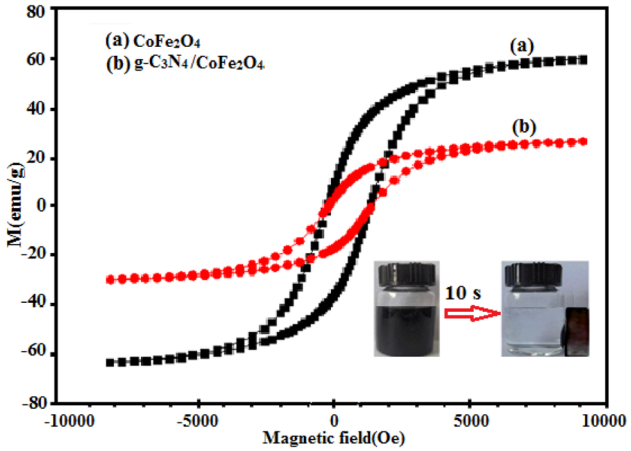

Fig. 8 Room-temperature magnetization curves of (a) $CoFe_2O_4$ and (b) g-C_3N_4/$CoFe_2O_4$ nanocomposite (inset: the magnetic separation of g-C_3N_4/$CoFe_2O_4$ nanocomposite by a magnet).

be attributed to the existence of non-magnetic g-C_3N_4 component. As can be seen in the inset of Fig. 8, the g-C_3N_4/$CoFe_2O_4$ nanocomposite could be easily separated from the water with a common magnet and quickly collected on the side of the glass vial, which indicates that this nanocomposite might be magnetically recycled from wastewater by an external magnetic field.

The g-C_3N_4/$CoFe_2O_4$ nanocomposite sample was subjected to determine the surface area, pore volume and corresponding pore-size distribution curve. As shown in Fig. 9(a) and (b), the N_2 adsorption–desorption isotherms display a typical type-IV curve with an H3-type hysteresis loop at a high relative pressure, which is associated with capillary condensation in mesopores (2 to 50 nm).[58] The data about the surface areas, pore volumes and average pore sizes of g-C_3N_4 nanosheets and g-C_3N_4/$CoFe_2O_4$ composite samples were summarized in Table 1. BET surface

Table 1 The texture parameters of C_3N_4 and g-C_3N_4/$CoFe_2O_4$ nanocomposite[a,b,c,d]

Sample	S_{BET} ($m^2\ g^{-1}$)	S_{Lan} ($m^2\ g^{-1}$)	V_{total} (cm^3/g)	D_p (nm)
C_3N_4	47.74	126.37	0.258	1.26
g-C_3N_4/$CoFe_2O_4$	93.66	143.39	0.415	12.60

[a] S_{BET}: BET surface area. [b] S_{Lan}: Langmuir surface area. [c] V_{total}: Total pore volume. [d] D_p: Average pore diameter estimated using the Barrett–Joyner–Halenda (BJH) method from the adsorption branch of the N_2 isotherms.

area and pore volume of g-C_3N_4/$CoFe_2O_4$ are found to be 93.66 $m^2\ g^{-1}$ and 0.415 $cm^3\ g^{-1}$, higher than those of g-C_3N_4 nanosheets (47.74 $m^2\ g^{-1}$ and 0.258 $cm^3\ g^{-1}$) which are benefit to the diffusion of electrolyte ions and the exposure of active sites. The pore size distribution of g-C_3N_4/$CoFe_2O_4$ composite in the inset of Fig. 9(b) presents a broad peak in the range from 5 to 20 nm. The high surface area and pore volume likely contribute to the high sonocatalytic activity. In summary, the high specific surface area provides more active sites, which may lead to the enhancement of sonocatalytic performance.

3.2. Sonocatalytic degradation of dyes

The sonocatalytic activity of g-C_3N_4/$CoFe_2O_4$ nanocomposite was investigated in degradation of some organic dye in aqueous solution under ultrasonic irradiation. The process was investigated by monitoring the characteristic absorption band of MB at about 665 nm. Initially, a suspension of g-C_3N_4/$CoFe_2O_4$ (0.66 g L^{-1}) in 50 mL of aqueous solution MB (25 mg L^{-1}) was exposed to ultrasonic (US) irradiation in the presence of H_2O_2 (0.1 mol L^{-1}). Fig. 10(a) shows the UV-vis absorbance spectra of MB aqueous solution in the presence of g-C_3N_4/$CoFe_2O_4$/H_2O_2/US system. It can be seen that the intensity of the absorption band at 665 nm decreases with the irradiation time and

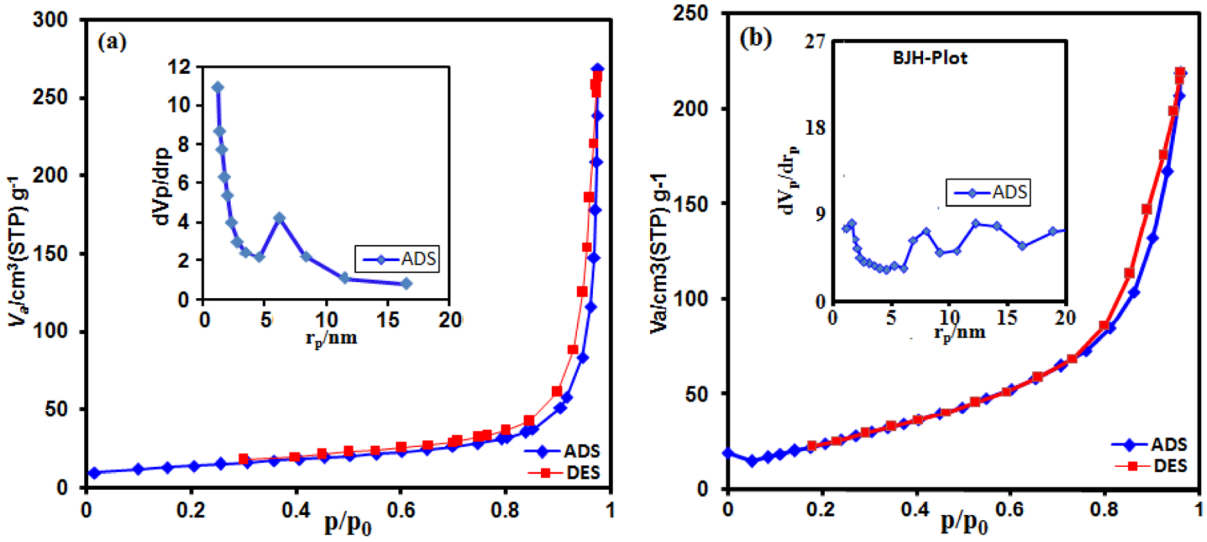

Fig. 9 N_2 adsorption–desorption isotherms of (a) C_3N_4 and (b) g-C_3N_4/$CoFe_2O_4$ nanocomposite. The insets are the pore size distribution curves.

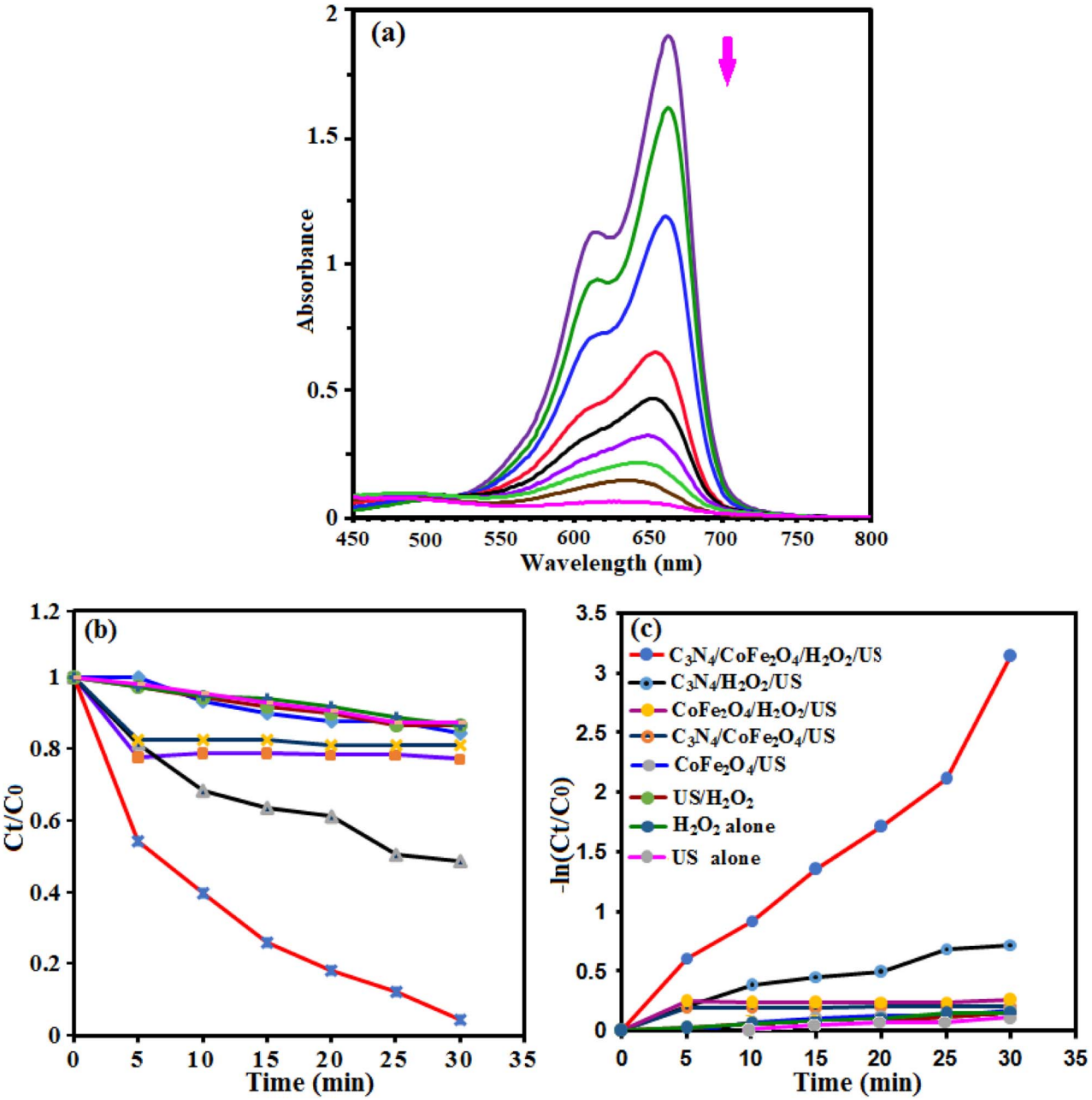

Fig. 10 (a) The UV-vis absorption changes, (b) concentration changes (C_t/C_0), and (c) the pseudo-first-order plots of $-\ln(C_t/C_0)$ as a function of irradiation time for MB sonodegradation in the presence of g-C_3N_4/$CoFe_2O_4$ nanocomposite. Conditions: $[MB]_0$ = 25 mg L^{-1},50 mL; $[H_2O_2]$ = 0.1 mol L^{-1}, 1 mL; [cat.] = 0.66 g L^{-1} at room temperature and natural pH = 7.

completely disappeared within 30 min. These findings confirmed the efficacy of the g-C_3N_4/$CoFe_2O_4$/H_2O_2/US system for successful degradation of MB dye. Fig. 10(b) shows the MB degradation (C/C_0) with the irradiation time over various catalysts which obviously reveals that the sonocatalytic activity of the g-C_3N_4/$CoFe_2O_4$/H_2O_2 is the highest among all samples under US. About 100% MB was degraded after 30 min over the g-C_3N_4/$CoFe_2O_4$ sample. The kinetic rate constants of the samples were obtained by plotting $-\ln C_t/C_0$ with time (in min) and the results are shown in Fig. 10(c). The sonocatalytic degradation of MB over the catalysts matches the pseudo-first-order kinetics equation ($-dC/dt = kC$). The rate constant, k, in different systems increased in the order of US alone (0.0046 min^{-1}) < H_2O_2 alone (0.0047 min^{-1}) < US/H_2O_2 (0.0052 min^{-1}) < $CoFe_2O_4$/US (0.0049 min^{-1}) < g-C_3N_4/$CoFe_2O_4$/US (0.0052 min^{-1}) < $CoFe_2O_4$/H_2O_2/US (0.0061 min^{-1}) < g-C_3N_4/H_2O_2/US (0.023 min^{-1}) < g-C_3N_4/$CoFe_2O_4$/H_2O_2/US (0.094 min^{-1}). The kinetic rate constant over g-C_3N_4/$CoFe_2O_4$ is 0.094 min^{-1}, which is 4 and15.4 times more than those of g-C_3N_4 (0.023 min^{-1}) and $CoFe_2O_4$ (0.0061 min^{-1}), respectively. Based on the comparison of different values of k, it can be shown that the combination of g-C_3N_4/$CoFe_2O_4$ nanocomposite

with ultrasonic irradiation and H_2O_2 has higher oxidation potential of MB degradation than the others, due to the synergistic effect between g-C_3N_4 and $CoFe_2O_4$ nanoparticles and the additional generation of reactive oxidizing species. The nanocomposite is an effective sonocatalyst for the degradation of MB and its efficiency degradation was 100% in the period of 30 min of irradiation.

3.2.1. Effect of enhancers. Several experiments were performed under identical conditions by using different enhancers for the degradation of MB in presence of the $CoFe_2O_4$/g-C_3N_4 nanocomposite. These experiments were done to study the effect of hydrogen peroxide, potassium periodate and peroxydisulfate with an initial concentration of 0.1 M on the sonodegradation efficiency of MB. And the results are shown in Fig. 11(a). Using the enhancers, interestingly increase the sonocatalytic degradation of MB. The degradation efficiency of MB dye in presence of the nanocomposite catalyst without any enhancer was 15% within 30 min. Also, the degradation efficiency of MB was 100% with hydrogen peroxide, peroxydisulfate and periodate within 30 min, 20 min and 15 min, respectively. By the addition of hydrogen peroxide, the sonocatalytic degradation of MB increases due to enhanced generation of $^{\bullet}OH$ radicals. The addition of peroxydisulfate can also increase the sonocatalytic degradation efficiency of MB due the generation of sulfate radicals and then the formation of $^{\bullet}OH$ radicals.[59] The addition of periodate ions produced the most effective sonocatalytic degradation of MB by capturing generated electrons.[60] Therefore, it is necessary to introduce an electron acceptor in this system. As a kind of electron acceptor, H_2O_2 is environment friendly and low cost, and it could be activated to general high reactive radical $^{\bullet}OH$ by accepting an electron.

3.2.2. Effect of hydrogen peroxide (H_2O_2) amount. The influence of H_2O_2 amount on the MB degradation was studied. As shown in Fig. 11(b), when the amount of H_2O_2 was increased from 0 to 2 mL, the degradation rate and efficiency increased from about 17% in 30 min to 100% within 20 min. The enhanced degradation rate of MB could be due to the more $^{\bullet}OH$ produced by increasing H_2O_2 amount.[61] However, further increase of the H_2O_2 amount (2.5 mL) led to slight reduction of the degradation rate and efficiency. The excessive H_2O_2 could scavenge $^{\bullet}OH$ to form less reactive species such as hydroperoxyl radical ($^{\bullet}OOH$), by which organic pollutants hardly are degraded.[62,63]

3.2.3. Effect of catalyst dosage. The catalyst dosage effect on the MB degradation was evaluated in solutions including the initial dosage range of 0–1 g L^{-1} nanocomposite and H_2O_2 (0.1 mol L^{-1}, 1 mL) for 30 min. The degradation efficiency of MB was about 10% after 30 min of sonoirradiation in the absence of the g-C_3N_4/$CoFe_2O_4$ nanocomposite. As shown in Fig. 11(c), the degradation efficiency increase with increasing the catalyst

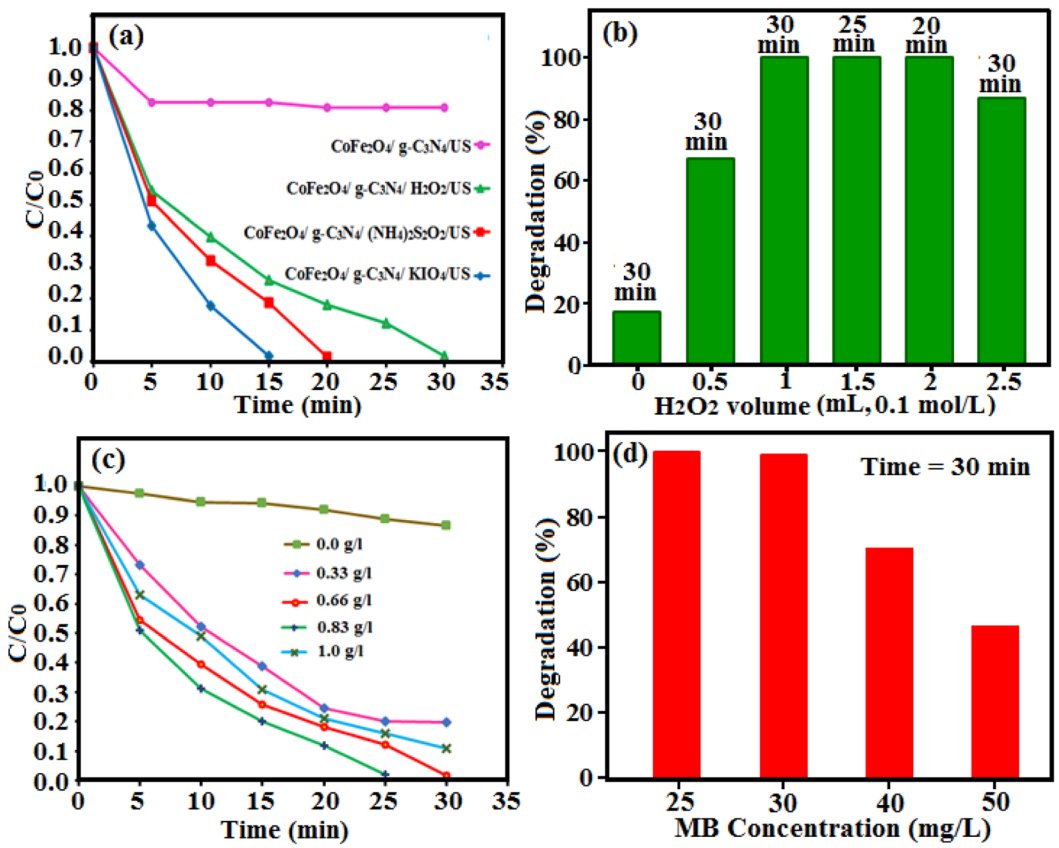

Fig. 11 Effects of (a) different enhancers, (b) the H_2O_2 amount, (c) the g-C_3N_4/$CoFe_2O_4$ sonocatalyst dosage, and (d) initial dye concentration on the sonocatalytic degradation of MB in the presence of g-C_3N_4/$CoFe_2O_4$ nanocomposite. Conditions: $[MB]_0$ = 25 mg L^{-1},50 mL; [enhancer] = 0.1 mol L^{-1}, 1 mL; [cat.] = 0.66 g L^{-1} at room temperature and natural pH = 7.

dosage from 0.33 to 0.83 g L^{-1}. With increasing the catalyst amount, more active sites and $^{\bullet}OH$ are formed on the catalyst surface for dye degradation.[64] However, more increase in the g-C_3N_4/$CoFe_2O_4$ nanocomposite dosage from 0.83 to 1 g L^{-1} results to reduce in degradation efficiency, due to the agglomeration of particles in the solution that reduces surface active sites for the production of $^{\bullet}OH$ radicals. In addition, the extent of cavitation phenomenon is related on the active surface area of the employed sonocatalyst. So, in the presence of the excess sonocatalyst, less ultrasonic waves could be conducted into the solution to generate cavitation bubbles.[65]

3.2.4. Effect of initial dye concentration. The effect of initial solution dye concentration on the sonoactivity was investigated, as it is an important parameter in the degradation of organic pollutants. Degradation efficiency of the g-C_3N_4/$CoFe_2O_4$ nanocomposite at various concentrations of MB from 25 to 50 mg L^{-1} was investigated and the results are illustrated in Fig. 11(d). The reaction time was fixed at 30 min, while all other parameters remained the same, as explained in the experimental section (50 mL dye solution, catalyst dosage: 0.66 g L^{-1} and H_2O_2: 0.1 M, 1mL). It was observed that MB degradation showed a significant decreasing trend from 100% to 43%, as the initial MB concentration enhanced from 25 to 50 mg L^{-1}, respectively. Based on the findings, the maximum degradation efficiency occurred at lower initial MB concentrations (25 and 30 mg L^{-1}) and was found to be 100% within 30 min, while, the degradation efficiency of about 70% and 43% was achieved for concentrations of 40 and 50 mg L^{-1} at the same time. This phenomenon would be attributed to some reasons: (i) an increase in competition between the intermediates and the parent compounds for the reaction with reactive oxidizing radicals, (ii) decreasing the generation rate of reactive species, because of filling the reactive sites by MB molecules and reducing the reactions between US irradiation and sonocatalyst and (iii) the degradation of all MB molecules would be impossible when the production rate of reactive oxidizing

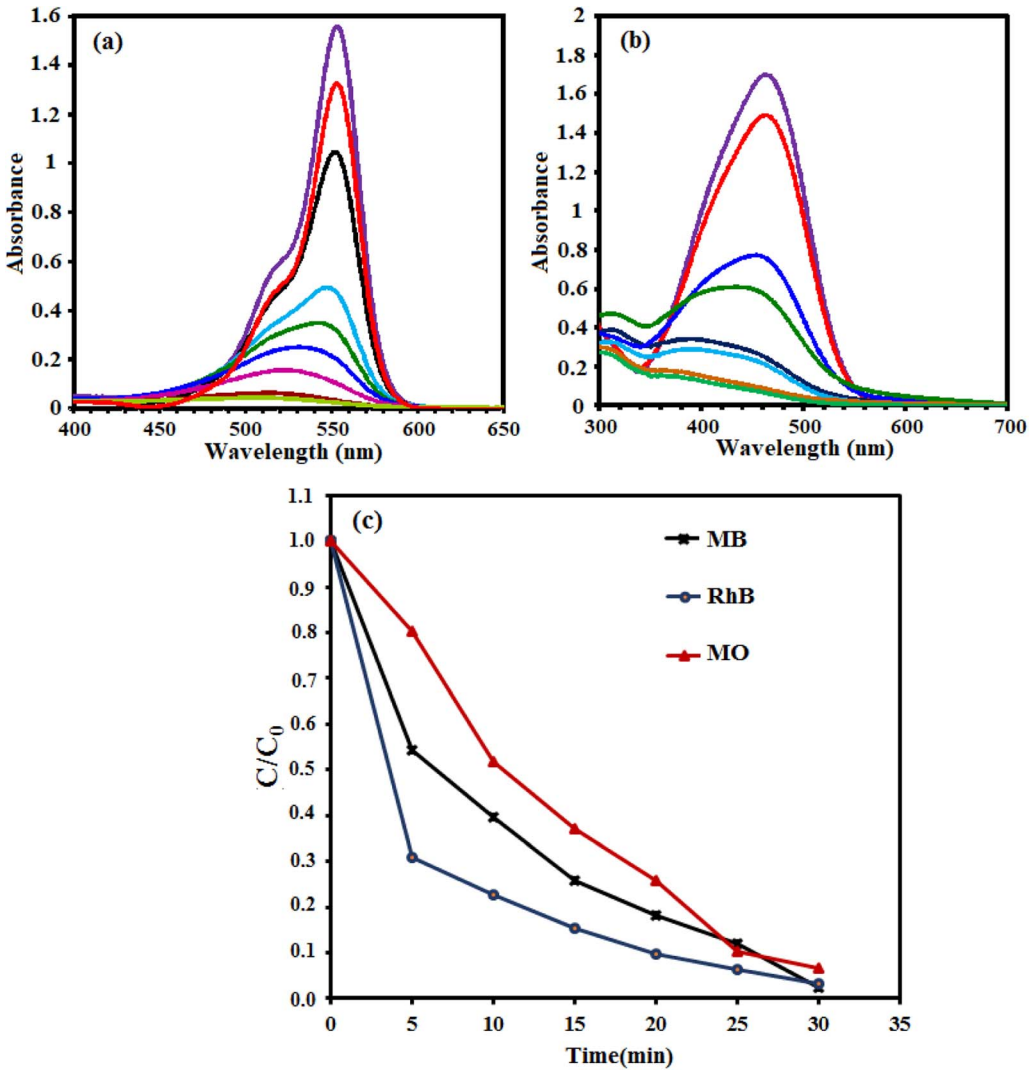

Fig. 12 The UV-vis absorption spectra changes of (a) rhodamine B (RhB), (b) methyl orange (MO), and (c) comparison of sonodegradation efficiency of dyes as a function of time over the g-C_3N_4/$CoFe_2O_4$ nanocomposite. Conditions: [dye] = 25 mg L^{-1}, 50 mL; [cat.] = 0.66 g L^{-1}; [H_2O_2] = 0.1 mol L^{-1}, 1 mL; at room temperature and natural pH = 7.

species is constant.[64–66] In contrast, at lower concentrations, a sufficient number of reactive oxidizing species is available in the solution for reaction with MB molecules that leads to high degradation rate.

3.2.5. Effect of initial solution pH. The effects of pH on sonocatalytic degradation efficiency of dyes were investigated Fig. 15 shows the degradation efficiency of MB dye after irradiation for 30 min at pH values from 3 to11. Degradation efficiency of 42%, 54%, 100%, 53% and 28 were reached at pH values of 3, 5, 7, 9 and 11, respectively. It is easily seen from these data that the degradation efficiency increases with increase in pH and exhibits maximum value at pH 7 and then decreases when the pH increases further to 9 and then 11. In more acidic and basic solutions, the catalyst's surface was covered with H^+ and OH^- ions, respectively. Therefore, the adsorption of H_2O_2 and dye molecules on the catalyst's surface will decrease. Moreover, the decomposition of H_2O_2 into H_2O and O_2 at basic conditions is very fast. All of the effects are detrimental to the catalytic crack of H_2O_2 by g-C_3N_4/$CoFe_2O_4$ to generate hydroxyl radicals. These results suggest that weak acidic and neutral initial pH values are beneficial for dye degradation. At neutral pH, the active sites on the catalyst's surface were free for the production of OH radicals resulting in the increase in the sonocatalytic MB degradation. The

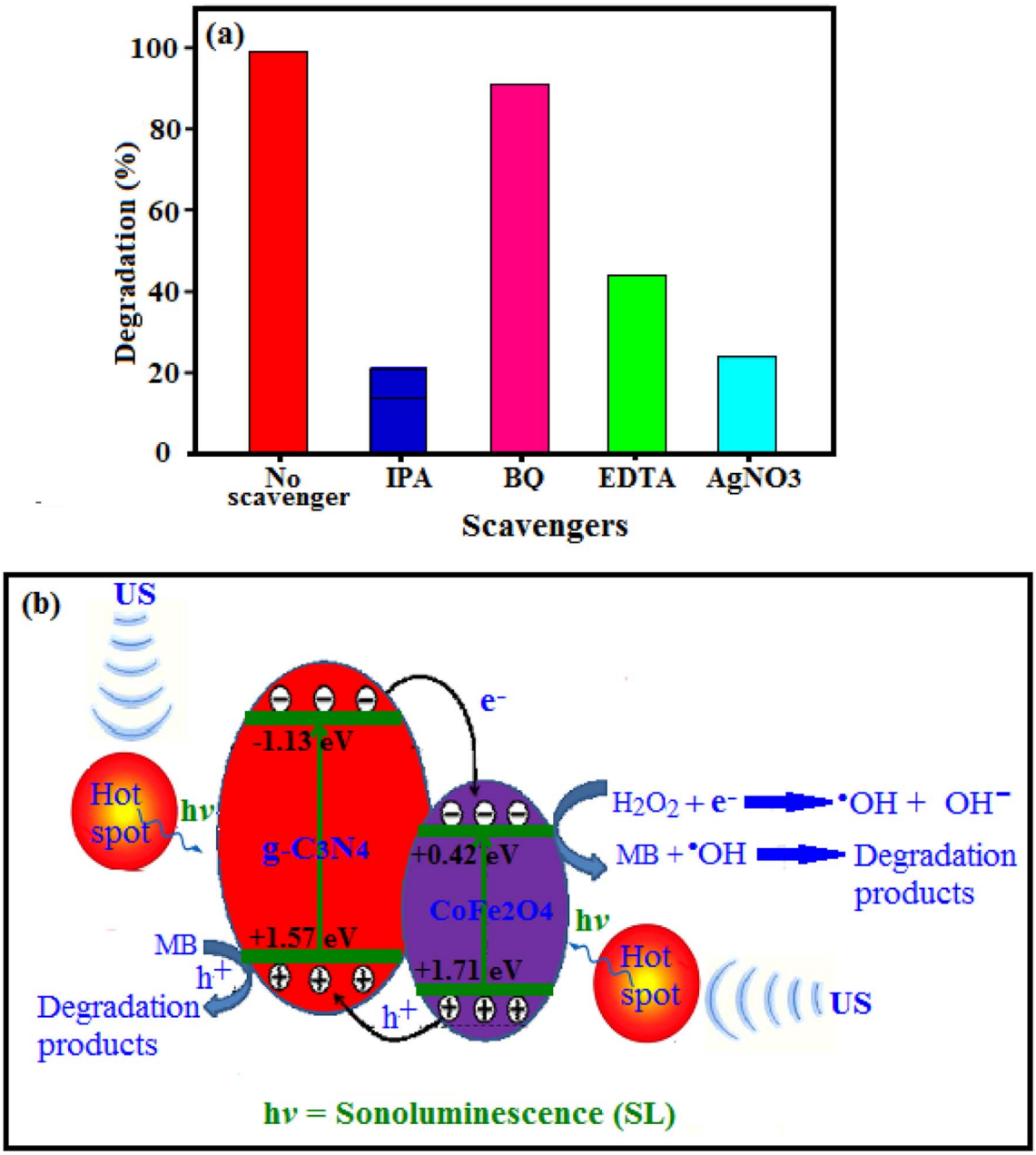

Fig. 13 (a) Effects of different scavengers on the sonocatalytic degradation of MB. Conditions: [MB] = 25 mg L^{-1}, 50 mL; [cat.] = 0.66 g L^{-1}; [H_2O_2] = 0.1 mol L^{-1}, 1 mL; [scavenger] = 0.1 mol L; at room temperature and natural pH = 7. (b) Schematic illustration of the possible sonocatalytic mechanism of the g-C_3N_4/$CoFe_2O_4$ nanocomposite under ultrasound irradiation.

experimental results depicted that the maximum MB degradation efficiency (100%) was taken place at pH 7 which was considered as an optimum value for subsequent experiments. It seems that greater accessibility of MB to active sites of catalyst resulted in a higher degradation efficiency of dye at natural pH level.

3.2.6. Effect of type of organic dyes. To investigate the activity of different dyes in the presence of the g-C_3N_4/$CoFe_2O_4$ nanocomposite, the degradation of rhodamine B (RhB) and methyl orange (MO) dyes was also investigated. The volume and concentration of the dye solutions were 50 mL and 30 mg L^{-1}, respectively. The amount of the g-C_3N_4/$CoFe_2O_4$ nanocomposite was 0.66 g L^{-1}. Fig. 12(a) and (b) show that the degradation efficiency of MO and RhB on the g-C_3N_4/$CoFe_2O_4$ nanocomposite were 94% and 100%, respectively. The lower degradation of MO molecules can be related to its high redox potential. As compared in Fig. 12(c), this novel sonocatalytic system exhibits excellent capacity for the degradation of various dyes under sono-irradiation.

3.2.7. Studies of sonocatalytic degradation mechanism. The active species participating in the sonocatalytic process were studied in order to elucidate the mechanism of sonocatalysis. The roles of the main active species were investigated through radical, hole and electron trapping experiments and the results are shown in Fig. 13(a). The different radical scavengers such as benzoquinone (BQ), ethylenediaminetetraacetic acid (EDTA), and isopropyl alcohol (IPA) were used to detect the production of superoxide radicals ($^{\bullet}O_2^-$), holes (h^+), and hydroxyl radicals ($^{\bullet}OH$) produced during the sonocatalysis process, respectively.[67] Also, $AgNO_3$ was used as a scavenger of electron (e^-). The degradation efficiency of MB decreased slightly upon the addition of benzoquinone (BQ), a scavenger to quench $^{\bullet}O_2^-$, indicating that dissolved $^{\bullet}O_2^-$ radicals were not the dominant active species in this process. In contrast, the addition of isopropyl alcohol (IPA, a hydroxyl radicals scavenger), the degradation efficiency had a significantly negative effect on the degradation of MB, confirming that dissolved $^{\bullet}OH$ radicals were the dominant active species. Upon the addition of disodium ethylenediaminetetraacetate (EDTA, a hole scavenger) the degradation efficiency dropped remarkably, confirming that the holes were another active species in the reactive system. Also, the degradation efficiency of MB significantly reduced because of the addition of $AgNO_3$ as a scavenger of e^- and the degradation rate of MB drops about 24%. It means that e^- plays a crucial role in the degradation of MB. The above results demonstrated that the sonocatalytic process was governed by direct holes, e^- and mainly $^{\bullet}OH^-$ oxidation reactions while free $^{\bullet}O_2^-$ radicals were negligible.[68]

The enhanced sonocatalytic activity can be ascribed to the formation of heterojunction between $CoFe_2O_4$ and C_3N_4. Based on the experimental results, possible mechanism of the MB sonodegradation over C_3N_4/$CoFe_2O_4$ nanocomposite under US irradiation was proposed. To show matching of energy levels of the $CoFe_2O_4$ and C_3N_4, their valence band (VB) and conduction band (CB) edge potentials were calculated by the Mulliken electronegativity theory using the following equations(eqn (1) and (2)):[69]

$$E_{CB} = \chi - E^e - 0.5E_g, \quad (1)$$

$$E_{VB} = E_{CB} + E_g \quad (2)$$

where χ and E_g denotes the absolute electronegativity and band gap, respectively. E^c is the energy of free electrons on the hydrogen scale (4.5 eV). Herein, the CB and VB edge potentials of g-C_3N_4 were calculated as −1.13 and +1.57 eV, respectively, while those for $CoFe_2O_4$ were calculated as +0.42 and +1.71 eV, respectively (represented in Fig. 13(b)). Due to their narrow band gaps, under the visible-light irradiation, $CoFe_2O_4$ and g-C_3N_4 are excited to produce some electron–hole pairs.[70]

On the basis of the above results and previous reports,[71–74] we propose the mechanisms of light absorption, charge transfer, and the reaction pathways for generating active radicals by g-C_3N_4/$CoFe_2O_4$ nanocomposites and the degradation of dyes as follows: As illustrated in Fig. 13(b), the ultrasonic cavitation effect produced the sonoluminescence which it could create lights with a wide wavelength range. The g-C_3N_4/$CoFe_2O_4$ nanocomposite can be excited by the produced lights with suitable wavelength and so this nanocomposite acting as a sonocatalyst to accomplish degradation (eqn (3)). In addition, the "hot spot" manufactured by ultrasonic cavitation effect in aqueous solution can possessed higher temperature than 1000 °C. Therefore, magnetic g-C_3N_4/$CoFe_2O_4$ nanocomposite can be excited by these hot spots. Also, high temperature could effectively decompose H_2O_2 molecules on the surface of the sonocatalyst to generate hydroxyl radicals ($^{\bullet}OH$). Since the CB of the g-C_3N_4 (−1.13 eV) is lower than CB of $CoFe_2O_4$ (+0.42 eV), so the excited-state electrons in the CB of g-C_3N_4 can be easily transfer into CB of $CoFe_2O_4$ (eqn (4)). However, The CB position of $CoFe_2O_4$ is much higher than the redox potential of $O_2/^{\bullet}O_2^-$ (−0.33 eV). So, the O_2 adsorbed on the surface of g-C_3N_4/$CoFe_2O_4$ won't be reduced. Therefore, it is necessary to introduce an electron acceptor in this system. As a kind of electron

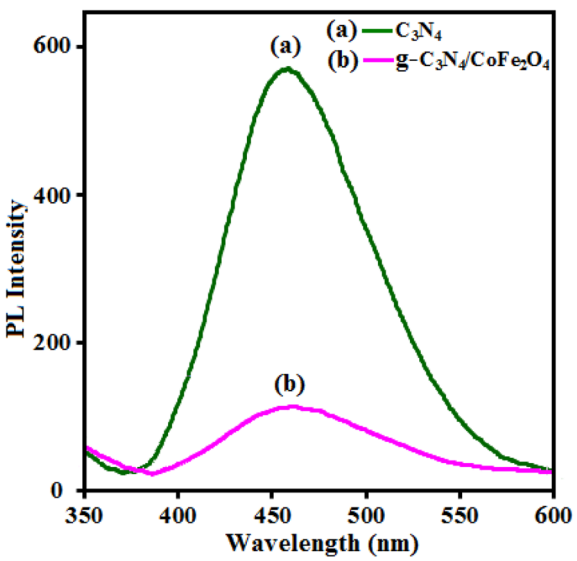

Fig. 14 PL spectra of (a) pure g-C_3N_4 and (b) g-C_3N_4/$CoFe_2O_4$ samples.

acceptor, H_2O_2 is environment friendly and it could be activated to general high reactive radical $^{\bullet}OH$ by accepting an electron (eqn (5)). Then, the electron in CB of $CoFe_2O_4$ can activate H_2O_2 to generate hydroxyl radical ($^{\bullet}OH$), which is a strong oxidizing agent to degrade MB (eqn (6)). In the other hand, due to VB position of $CoFe_2O_4$ (+1.71 eV) is more than of g-C_3N_4 (+1.57 eV), the produced sonogenerated holes (h^+) at the VB of $CoFe_2O_4$ will inject to that of g-C_3N_4. These sonogenerated holes in the VB of g-C_3N_4 can oxidize organic dyes adsorbed onto the surface of the catalyst directly (eqn (7)). The reactions are summerized as follows (eqn (3)–(7)):

$$\text{g-}C_3N_4/CoFe_2O_4 + US \rightarrow \text{g-}C_3N_4(h^+, e^-) + CoFe_2O_4(h^+, e^-) \quad (3)$$

$$\text{g-}C_3N_4(h^+, e^-) + CoFe_2O_4(h^+, e^-) \rightarrow \text{g-}C_3N_4(h^+) + CoFe_2O_4(e^-) \quad (4)$$

$$CoFe_2O_4(e^-) + H_2O_2 \rightarrow {}^{\bullet}OH + OH^-, \quad (5)$$

$$MB + {}^{\bullet}OH \rightarrow CO_2 + H_2O + \ldots \quad (6)$$

$$\text{g-}C_3N_4(h^+) + MB \rightarrow \text{g-}C_3N_4 + MB^{\bullet+} \rightarrow CO_2 + H_2O + \ldots \quad (7)$$

To justify the proposed path for the g-C_3N_4/$CoFe_2O_4$ nanocomposites towards sonocatalytic degradation, a photoluminescence (PL) study is an effective and informative technique that can give a better understanding of the electron flow and charge separation mechanism of the sonocatalyst. The higher fluorescence intensity means more recombination of electron–hole pairs and lower catalytic activity and a weak peak indicates better electron–hole pair separation.[75] Fig. 14 shows the room-temperature PL spectra of the pristine g-C_3N_4 and the g-C_3N_4/$CoFe_2O_4$ hybrid material excited at 350 nm. Fig. 14(a)

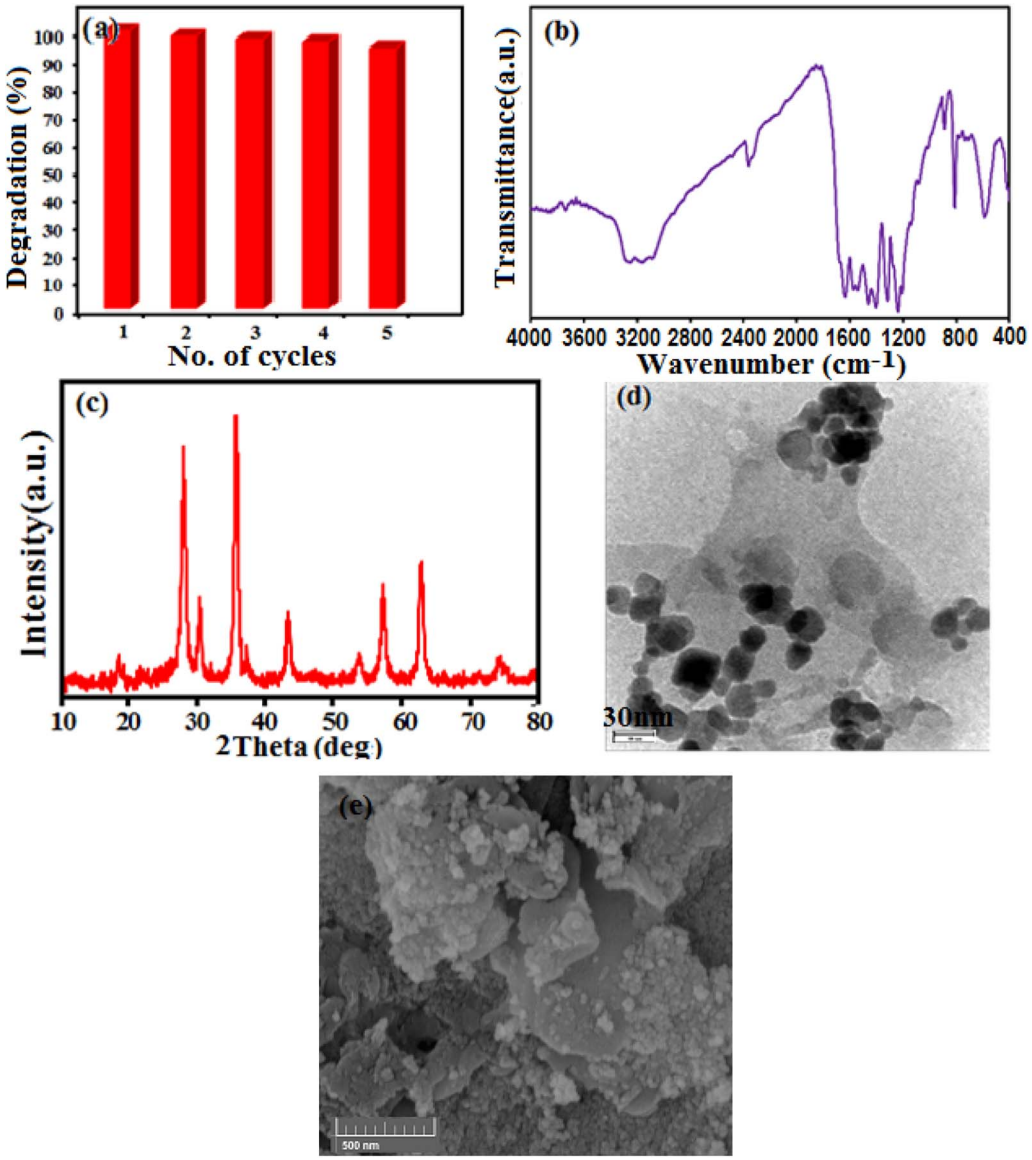

Fig. 15 (a) Cycling runs of g-C_3N_4/$CoFe_2O_4$ nanocomposite in the sonodegradation of MB. Each run of photocatalytic reactions lasted for 30 min. (b) FT-IR spectrum, (c) XRD pattern and (d) TEM image (e) SEM image of the recovered nanocomposite after the 5th run.

shows the PL spectrum the pristine g-C_3N_4 nanosheets with high intensity at about 460 nm, indicating high electron–hole recombination.[76,77] For g-C_3N_4/$CoFe_2O_4$ hybrid material in Fig. 14(b), the position of the emission peak in the PL spectrum was similar to that of the pure g-C_3N_4, but the emission intensity significantly decreased. This demonstrated that the recombination of photo-generated charge carriers was greatly inhibited by the introduction of $CoFe_2O_4$, which showed the photogenerated electron–hole pairs in g-C_3N_4/$CoFe_2O_4$ hybrid material had higher separation efficiency than those in the pure g-C_3N_4.[78] This led to better utilization of electron and hole pairs induced by light irradiation. The PL result is in accordance with the sonocatalytic activity of the catalyst.

3.2.8. Reusability and stability of g-C_3N_4/$CoFe_2O_4$. The stability of the catalyst materials is a significant factor in the catalytic experiments. The synthesized nanocomposite is insoluble in water, therefor, the catalyst can be separated by external magnetic field, washed with water and ethanol, dried at 60 °C and then employed for the degradation of MB up to five cycles. As can be seen in Fig. 15(a), the obtained results indicated negligible decrease of its sonocatalytic activity after five repeated cycles. The amounts of Co and Fe metals in the filtrate were also determined to be about less than 0.1% by ICP-AES analysis. Based on Fig. 15(b)–(e), there is no noticeable change in the FT-IR spectrum, XRD pattern and TEM-SEM images of the sonocatalyst before and after the 5th cycle. These findings confirm the composite has a good stability during the sonocatalytic degradation of dyes.

4. Conclusion

In summary, the g-C_3N_4/$CoFe_2O_4$ nanocomposite was synthesized by a simple hydrothermal method. The FT-IR, XRD and EDX analyses confirmed the successful synthesis of the g-C_3N_4/$CoFe_2O_4$ nanocomposite. The TEM and SEM photographs of the nanocomposite revealed that the spherical of $CoFe_2O_4$ nanoparticles were anchored on the surface of the g-C_3N_4 naosheets. Also, the nanocomposite was used to degrade organic dyes including MB, MO and RhB. Efficient sonocatalyst degradation was 100% for the removal of dyes. Due to magnetic properties of the g-C_3N_4/$CoFe_2O_4$ nanocomposite, it could be easily separated from the aqueous solutions with a magnet. This study established a low-cost, green and easy heterogeneous catalyst for the degradation of organic dyes and other pollutants in wastewater.

Conflicts of interest

There are no conflicts of interest to declare.

Acknowledgements

The authors gratefully acknowledge the Lorestan University and Iran Nanotechnology Initiative Council (INIC) for their financial support.

References

1 M. Saranya, R. Ramachandran, E. J. J. Samuel, S. K. Jeong and A. N. Grace, *Powder Technol.*, 2015, **279**, 209–220.
2 K. Ji, J. Deng, H. Zang, J. Han, H. Arandiyan and H. Dai, *Appl. Catal., B*, 2015, **165**, 285–295.
3 Y. Xia, Z. He, Y. Lu, B. Tang, S. Sun, J. Su and X. Li, *RSC Adv.*, 2018, **8**, 5441–5450.
4 M. Bartolomeu, M. G. P. M. S. Neves, M. A. F. Faustino and A. Almeida, *Photochem. Photobiol. Sci.*, 2018, **17**, 1573–1598.
5 D. Kanakaraju, B. D. Glass and M. Oelgemöller, *J. Environ. Manage.*, 2018, **219**, 189–207.
6 R. Andreozzi, V. Caprio, A. Insola and R. Marotta, *Catal. Today*, 1999, **53**, 51–59.
7 N. N. Mahamuni and Y. G. Adewuyi, *Ultrason. Sonochem.*, 2010, **17**, 990–1003.
8 M. Kurian, *Cleaner Eng. Technol.*, 2021, **2**, 100090.
9 I. Hua and M. R. Hoffmann, *Environ. Sci. Technol.*, 1996, **30**, 864–871.
10 P. Chowdhury and T. Viraraghavan, *Sci. Total Environ.*, 2009, **407**, 2474–2492.
11 H. Ferkous, O. Hamdaoui and S. Merouani, *Ultrason. Sonochem.*, 2015, **26**, 40–47.
12 R. Balachandran, Z. Patterson, P. Deymier, S. A. Snyder and M. Keswani, *Chemosphere*, 2016, **147**, 52–59.
13 E. A. Serna-Galvis, J. Silva-Agredo, A. L. Giraldo-Aguirre and R. A. Torres-Palma, *Sci. Total Environ.*, 2015, **524–525**, 354–360.
14 S. Goskonda, W. James Catallo and T. Junk, *Waste Manag.*, 2002, **22**, 351–356.
15 T. Sivasankar and V. S. Moholkar, *Ultrason. Sonochem.*, 2009, **16**, 769–781.
16 K. S. Suslick, S. J. Doktycz and E. B. Flint, *Ultrasonics*, 1990, **28**, 280–290.
17 K. Yasui, T. Tuziuti, J. Lee, T. Kozuka, A. Towata and Y. Iida, *J. Chem. Phys.*, 2008, **128**, 184705.
18 K. S. Suslick, Y. Didenko, M. M. Fang, T. Hyeon, K. J. Kolbeck, W. B. McNamara, M. M. Mdleleni and M. Wong, *Philos. Trans. R. Soc., A*, 1999, **357**, 335–353.
19 J. Lifka, B. Ondruschka and J. Hofmann, *Eng. Life Sci.*, 2003, **3**, 253–262.
20 C. Petrier, Y. Jiang and M. F. Lamy, *Environ. Sci. Technol.*, 1998, **32**, 1316–1318.
21 N. N. Mahamuni and Y. G. Adewuyi, *Ultrason. Sonochem.*, 2010, **17**, 990–1003.
22 Y. L. Pang, A. Z. Abdullah and S. Bhatia, *Desalination*, 2011, **277**, 1–14.
23 P. Qiua, B. Parka, J. Choia, B. Thokchomb, A. B. Panditc and J. Khima, *Ultrason. Sonochem.*, 2018, **45**, 29–49.
24 Z. Eren, *J. Environ. Manage.*, 2012, **104**, 127–141.
25 Z. Eren and N. H. Ince, *J. Hazard. Mater.*, 2010, **177**, 1019–1024.
26 U. S. Jonnalagadda, X. Su and J. J. Kwan, *Ultrason. Sonochem.*, 2021, **73**, 105530.
27 S. Cao, J. Low, J. Yu and M. Jaroniec, *Adv. Mater.*, 2015, **27**, 2150–2176.

28 L. H. Amorin, V. Y. Suzuki, N. H. de Paula, J. L. Duarte, M. A. T. da Silva, C. A. Taft and F. de Almeida La Porta, *New J. Chem.*, 2019, **43**, 13647–13653.
29 W. J. Ong, L. L. Tan, Y. H. Ng, S. T. Yong and S.-P. Chai, *Chem. Rev.*, 2016, **116**, 7159–7329.
30 K. Xu, H. Xu, G. Feng and J. Feng, *New J. Chem.*, 2017, **41**, 14602–14609.
31 M. Ismael and Y. Wu, *New J. Chem.*, 2019, **43**, 13783–13793.
32 S. Bhowmik, S. J. Phukan, N. K. Sah, M. Roy, S. Garai and P. K. Iyer, *ACS Appl. Nano Mater.*, 2021, **4**, 12845–12890.
33 R. Suresh, S. Rajendran, P. S. Kumar, D. V. N. Vo and L. Cornejo-Ponce, *Chemosphere*, 2021, **274**, 129734.
34 B. Palanivel, S. devi Mudisoodum perumal, T. Maiyalagan, V. Jayarman, C. Ayyappan and A. Mani, *Appl. Surf. Sci.*, 2019, **498**, 143807.
35 B. Palanivel, C. Ayyappan, V. Jayarman, S. Chidambaram, R. Maheswaran and A. Mani, *Mater. Sci. Semicond. Process.*, 2019, **100**, 87–97.
36 R. Cheng, X. Fan, M. Wang, M. Li, J. Tian and L. Zhang, *RSC Adv.*, 2016, **6**, 18990–18995.
37 S. Huang, Y. Xu and H. Li, *Colloids Surf., A*, 2015, **478**, 71–80.
38 H. Ji, X. Jing and H. Li, *RSC Adv.*, 2015, **5**, 57960–57967.
39 S. Zhang, J. Li and X. Wang, *ACS Appl. Mater. Interfaces*, 2013, **5**, 12735–12743.
40 Y. Yao, F. Lu and S. Wang, *J. Hazard. Mater.*, 2015, **297**, 224–233.
41 Y. Liu, Y. Song, Y. You, X. Fu, J. Wen and X. Zheng, *J. Saudi Chem. Soc.*, 2017, **22**, 439–448.
42 J. Liu, T. Zhang, Z. Wang, G. Dawson and W. Chen, *J. Mater. Chem.*, 2011, **21**, 14398–14401.
43 G. Li, N. Yang, W. Wang and W. Zhang, *J. Phys. Chem. C*, 2009, **113**, 14829–14833.
44 X. Li, J. Zhang, L. Shen, Y. Ma, W. Lei, Q. Cui and G. Zou, *Appl. Phys. A: Mater. Sci. Process.*, 2009, **94**, 387–392.
45 M. Kim, S. Hwang and J.-S. Yu, *J. Mater. Chem.*, 2007, **17**, 1656–1659.
46 H. Yan and H. Yang, *J. Alloys Compd.*, 2011, **509**, L26–L29.
47 J. Deng, Y. Shao, N. Gao, C. Tan, S. Zhou and X. Hu, *J. Hazard. Mater.*, 2013, **262**, 836–844.
48 J. Xu, Y. Wang and Y. Zhu, *Langmuir*, 2013, **29**, 10566–10572.
49 F. Dong, Y. Sun, L. Wu, M. Fu and Z. Wu, *Catal. Sci. Technol.*, 2012, **2**, 1332–1335.
50 L. Jing, Y. Xu, S. Huang, M. Xie, M. He, H. Xu, H. Li and Q. Zhang, *Appl. Catal., B*, 2016, **199**, 11–22.
51 T. Aghavnian, J. B. Moussy, D. Stanescu, R. Belkhou, N. Jedrecy, H. Magnan, P. Ohresser, M. A. Arrio, P. Sainctavit and A. Barbier, *J. Electron Spectrosc. Relat. Phenom.*, 2015, **202**, 16–21.
52 G. Song, F. Xin and X. Yin, *J. Colloid Interface Sci.*, 2015, **442**, 60–66.
53 P. S. Yoo, D. Amaranatha Reddy, Y. Jia, S. E. Bae, S. Huh and C. Liu, *J. Colloid Interface Sci.*, 2017, **486**, 136–143.
54 Y. Xu, Q. Liu, C. Liu, Y. Zhai, M. Xie, L. Huang, H. Xu, H. Li and J. Jing, *J. Colloid Interface Sci.*, 2017, **512**, 555–566.
55 A. A. Rodriguez-Rodriguez, S. Martinez-Montemayor, C. C. Leyva-Porras, F. E. Longoria-Rodriguez, E. Martinez-Guerra and M. Sanchez-Dominguez, *J. Nanomater.*, 2017, **2017**, 1–15.
56 S. Min and G. Lu, *J. Phys. Chem. C*, 2012, **116**, 19644–19652.
57 A. Ren, C. B. Liu, Y. Z. Hong, W. D. Shi, S. Lin and P. Li, *Chem. Eng. J.*, 2014, **258**, 301–308.
58 L. Li, S. Xiang, S. Cao, J. Zhang, G. Ouyang, L. Chen and C. Y. Su, *Nat. Commun.*, 2013, **4**, 1774.
59 A. Khataee, A. Karimi, S. Arefi-Oskoui, R. D. C. Soltani, Y. Hanifehpour, B. Soltani and S. W. Joo, *Ultrason. Sonochem.*, 2015, **22**, 371–381.
60 J. Jiang, J. Zou, L. Zhu, L. Huang, H. Jiang and Y. Zhang, *J. Nanosci. Nanotechnol.*, 2011, **11**, 4793–4799.
61 M. Xia, M. Long, Y. Yang, C. Chen, W. Cai and B. Zhou, *Appl. Catal., B*, 2011, **110**, 118–125.
62 F. X. Wang, Y. L. Chen, R. S. Zhu and J. M. Sun, *Dalton Trans.*, 2017, **47**, 11306–11317.
63 S. Valizadeh, M. H. Rasoulifard and M. S. Seyed Dorraji, *Appl. Surf. Sci.*, 2014, **319**, 358–366.
64 N. Ertugay and F. N. Acar, *Appl. Surf. Sci.*, 2014, **318**, 121–126.
65 A. Khataee, S. Saadi, B. Vahid, S. W. Joo and B. K. Min, *Ultrason. Sonochem.*, 2016, **29**, 27–38.
66 H. Zhang, C. Wei, Y. Huang and J. Wang, *Ultrason. Sonochem.*, 2016, **30**, 61–69.
67 M. C. Yin, Z. S. Li, J. H. Kou and Z. G. Zou, *Environ. Sci. Technol.*, 2009, **43**, 8361–8366.
68 F. Wang, H. Yang and Y. C. Zhang, *Mater. Sci. Semicond. Process.*, 2018, **73**, 58–66.
69 C. Yu, H. He, W. Zhou, Z. Liu and L. Wei, *Sep. Purif. Technol.*, 2019, **217**, 137–146.
70 H. He, Z. Luo and C. Yu, *J. Alloys Compd.*, 2020, **816**, 152652.
71 P. Qiu, W. Li, K. Kang, B. Park and W. Luo, *J. Mater. Chem. A*, 2014, **2**, 16452–16458.
72 L. Nirumand, S. Farhadi, A. Zabardasti and A. Khataee, *Ultrason. Sonochem.*, 2018, **42**, 647–658.
73 H. He, J. Li, C. Yu and Z. Luo, *Sustainable Mater. Technol.*, 2019, **22**, e00127.
74 H. He, L. Zeng, X. Peng, Z. Liu, D. Wang, B. Yang, Z. Li, L. Lei, S. Wang and Y. Hou, *Chem. Eng. J.*, 2023, **451**, 138628.
75 J. Hu, C. Chen, H. Yang, F. Yang, J. Qu, X. Yang, W. Sun, L. Dai and C. M. Li, *Appl. Catal., B*, 2022, **317**, 121723.
76 T. Yang, Y. Shao, J. Hu, J. Qu, X. Yang, F. Yang and C. M. Li, *Chem. Eng. J.*, 2022, **448**, 137613.
77 S. Vadivel, D. Maruthamani, A. Habibi-Yangjeh, B. Paul, S. Sankar-Dhar and K. Selvam, *J. Colloid Interface Sci.*, 2016, **480**, 126–136.
78 X. Li, J. Hu, T. Yang, X. Yang, J. Qu and C. M. Li, *Nano Energy*, 2022, **92**, 106714.